

# 2nd CEPHONA Workshop on Microscopic Characterisation of Materials and Structures for Photonics

Warsaw, November 22-23, 2004

## APPLICATION OF RAMAN-SPECTROSCOPY TO ANALYTICAL PURPOSES AT SEMICONDUCTOR STRUCTURES AND DEVICES

Jens W. Tomm

*Max-Born-Institut für Nichtlineare Optik und Kurzzeitspektroskopie Berlin (MBI)  
Max-Born-Str. 2 A, D-12489 Berlin, Germany*

### ABSTRACT

After a brief introduction we discuss examples for the application of Raman spectroscopy. First the potential of Raman spectroscopy to for analysis of technological processes such as ion implantation and annealing is addressed. A second group of experiments is devoted to the application of this kind of spectroscopy to strain analysis in devices and to facet temperature measurements at operating diode lasers.

### 1. INTRODUCTION

If light interacts with solids, such as semiconductors, a number of elementary processes take place such as reflection, absorption as well as elastic and inelastic scattering. The Raman process represents the inelastic scattering of photons at elementary excitations such as phonons, plasmons or localized defects. A phonon is Raman-active if the first derivative of the polarizability with respect to the vibrational normal coordinate has a non-zero value. A phonon can be either IR or Raman active, however, only in crystals without center of inversion. The corresponding selection rules for the Raman scattering processes at phonons, however, are frequently violated if complex heterostructures or quantum-wells (QW) are considered.

In this Lecture we first deal with several applications of Raman analysis. First we discuss effects related to technological processes such as ion-implantation and rapid thermal annealing and their impact on Raman spectra. In the second part we address the use of micro ( $\mu$ ) Raman spectroscopy for the analysis of strain profiles along device structures. The third part is on the use of this technique as a unique 'micro-thermometer'. After a methodological introduction into this kind of surface temperature measurement, a number of practical examples of  $\mu$ Raman investigations at facets of diode lasers are presented. This involves investigations of devices with and without current blocking layers at the front facet and the monitoring of facet temperatures versus operation time in long-term aging experiments. Furthermore, we discuss investigations of the facet temperatures of quantum-dot (QD) lasers. We show that QD lasers have lower facet temperatures for similar operation conditions compared to conventional QW lasers. Experimental and methodological issues as well as practical limitations will be addressed, too.

## 2. EXPERIMENTAL

For the experiments that are discussed in this Lecture we use as the excitation the 514.5 nm line of an Ar-ion laser, which is focused onto the test device by using a microscope. A spot diameter of  $\sim 1 \mu\text{m}$ , which is determined by using the knife-edge method at a GaInP/GaA-heterointerface, is achieved. The back-scattered light from the sample is collected through the same microscope, then fed into the  $f=0.6 \text{ m}$  Raman triple-path spectrometer (DILOR x-y, 600 and 1800 grooves/mm) and detected with a liquid-nitrogen-cooled CCD matrix camera. Measurements are done either by making use of the triple monochromator system or by employing only one of three monochromators and introducing an additional notch-filter. The selection of the operation mode very much depends on the particular experiment and the sample. Typically, the energetic distance between a reference plasma line of the excitation laser and a phonon line is analyzed, e.g., by using lineshape fits.

## 3. PROPERTIES OF $\text{As}^+$ -IMPLANTED AND ANNEALED GaAs AND InGaAs QWs

Ion implantation is one basic technique in solid-state technology, which is used in mass production for several purposes such as post-growth doping, creation of insulating layers, and carrier-pair-lifetime engineering. There are several studies that employ, among others, Raman spectroscopy for studying the impact of implantation and, to some extent, subsequent annealing. These reports reveal at least one common experimental fact: Ion implantation causes a low-energy-shift of the phonon Raman lines that may be compensated, depending on the conditions chosen, either in part or almost completely by annealing. The presence of the low-energy shift is independent of implantation doses, energies and the species that is implanted, e.g. O [1], Si [2], Ar [3], Be [4], As [5], P [6], and H [7], whereas the magnitude of the low-energy-shift is governed by these parameters. The following interpretations for the shift are suggested:

- (i) Tensile strain: Tensile strain is well-known to reduce phonon energies [8], see, e.g., in Si [9] or GaAs [7], [10].
- (ii) Anharmonicity in the vibrational potential according to the explanations outlined in Refs. [6] and [11].
- (iii) Phonon confinement, i.e. the ‘spatial correlation model’. The finite size of regions that are assumed to be formed during implantation hinder the free propagation of phonons resulting in a

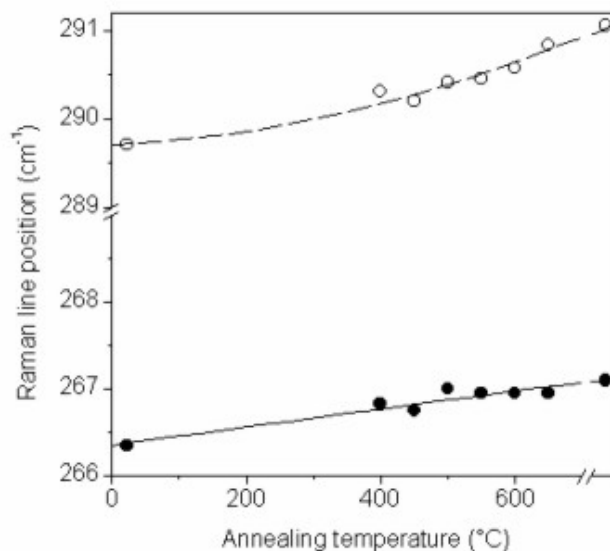


Fig. 1. Spectral position of the LO- (open circles) and TO-phonon peaks (full circles) arising from the GaAs-like modes from both the bulk-like GaAs cap as well as from the QW versus rapid thermal annealing temperature. Data from the as-grown sample are shown at the right behind the axis break of the abscissa. Data from the as-implanted sample are presented at ambient temperature.

range of allowed q-values out of the zone centre. According to the analysis suggested by Tiong et al. [5], cf. also references therein, one obtains a localization length that is attributed to the diameter of unperturbed crystalline areas, which might be generically identified by a ‘grain size’ that corresponds to the spatial correlation length.

Figure 1 illustrates the implantation and annealing behavior of a 9.5 nm thick compressively strained  $\text{In}_{0.253}\text{Ga}_{0.747}\text{As}$  QW ( $\Delta a/a = -1.8123\%$ ) and the surrounding GaAs, in particular the 66 nm thick GaAs cap layer. The structure was then  $\text{As}^+$ -implanted with an acceleration energy of 150 keV and a fluence of  $3.5 \times 10^{12} \text{ cm}^{-2}$ . Then the wafer was cleaved into several parts, which experienced a rapid thermal annealing process for 60 s at different temperatures. The result shown in Fig. 1 exactly reproduces the earlier findings in the literature, namely a low-energy shift of the phonon lines with implantation, which is at least partly relaxed by annealing. Furthermore, it is visible that the LO-line shifts stronger than the TO-line. In order to check the assumption about the creation of tensile strain

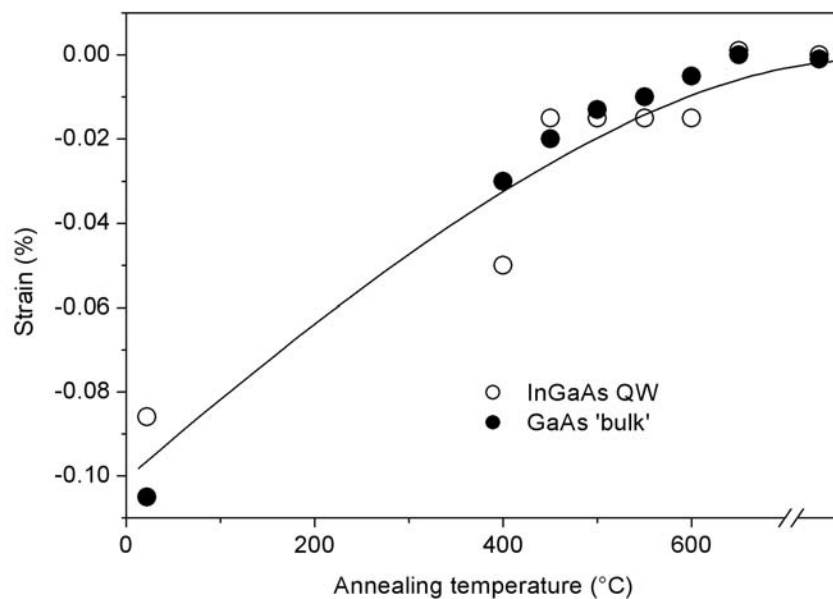


Fig. 2. Deformation of the GaAs cap (full circles) and the  $\text{In}_{0.253}\text{Ga}_{0.747}\text{As}$  QW (open circles) obtained by modeling of high resolution X-ray diffraction pattern. The biaxial  $\varepsilon = -1.812\%$  built-in strain of the QW on GaAs was set to zero for this display. The line is a guide to the eye.

caused by the implantation, we perform strain measurements by using the high resolution X-ray diffraction technique. The results are shown in Fig. 2. From the lattice constant changes measured by high resolution X-ray diffraction it becomes clear that implantation causes compressive strain most likely by the creation of native defects that compress the lattice. Thus the observed Raman-shifts are not caused by tensile strain. The ‘spatial correlation model’, however, provides concordant quantitative explanations for both the shift as well as for the observed lineshape changes of the phonon peaks. The latter are not discussed here.

Furthermore, this model also explains, why the LO-line shifts stronger than the TO-line. Considering the dispersion curves of the optical phonon branches, the dispersion of LO-phonons at the zone center is stronger than the one of TO-phonons. Thus, in the restricted k-range around the zone center that is defined by the implantation-induced damage, a stronger reduction of the LO-phonon energy is expected than for the TO-phonon energy. Thus a clarification of the nature of the implantation induced Raman-line shift is achieved. It should be noted that this low-energy shift overcompensates the shift to higher phonon energies that is caused by the lattice compression due to defect creation; see Fig. 2.

#### 4. RAMAN ANALYSIS OF STRAIN IN PACKAGED DIODE LASERS

As mentioned before the Raman-technique is sensible to strain. Mechanical strain is known to be involved in almost all semiconductor heterostructures. This strain, which is caused by the different lattice constants of the different materials in such a structures, is called built-in strain and is typically of biaxial symmetry. Device packaging might introduce additional strains. This is the case, e.g., if a semiconductor chip is soldered on a heat sink that has an other thermal expansion coefficient as the chip material itself. For a special device group, the so-called ‘cm-bar’ high-power diode laser arrays, this kind of soldering is required in order to achieve an efficient thermal coupling of the chip to the

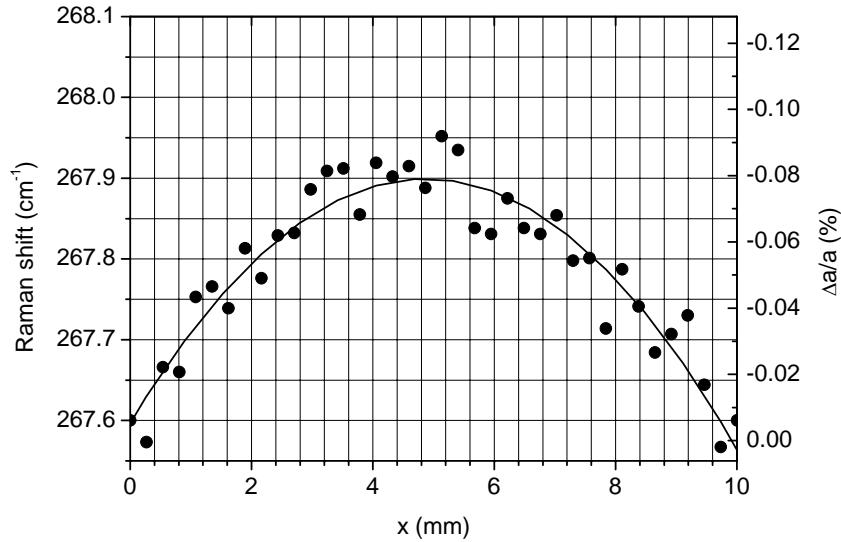


Fig. 3. Micro-Raman line position along a test ‘cm-bar’. The strain scale  $\Delta a/a$ , cf. right ordinate, was obtained by using equation  $\Delta\omega_{\text{TO}} = -410 \text{ cm}^{-1} \times \Delta a/a$  assuming the device edge to be unstrained.

heatsink. For the special device geometry of these ultra-wide arrays (width 1 cm, cavity length 0.9-1.5 mm) it turns out that the packaging predominantly introduces uniaxial compressive stress along the 110-direction [12, 13]. Fig. 3 shows the Raman-line position versus the local position along such a ‘cm-bar’ high-power diode laser array. By using

$$\Delta\omega_{\text{TO}} = -410 \text{ cm}^{-1} \times \Delta a/a \quad (1)$$

according to Ref. [14], a scale indicating the relative change of the lattice constant  $\Delta a/a$  versus local position is added at the right ordinate. Here the packaging induced strain at the device edges ( $x=0$  and  $10 \text{ mm}$ ) was set to zero, being in agreement with both model calculations [12] and experiments [15]. Thus  $\mu$ Raman-spectroscopy demonstrates the ability to reveal strain fields in devices. In our particular case, even the spatial modulation of the packaging-induced strain, which may be orders of magnitude smaller than the built-in strain, is clearly shown.

#### 5. RAMAN FACET TEMPERATURE MEASUREMENTS AT OPERATING DIODE LASERS

In addition to the sensitivity to stress and strain, the Raman-technique is also sensitive to temperature variation. The extremely small volume from which the spectra are collected (excitation spot  $\varnothing \sim 1 \mu\text{m}$ , information depth  $\sim 100 \text{ nm}$ ) makes  $\mu$ Raman a unique ‘micro-thermometer’. There are two independent ‘information channels’ that allow to get temperature data out of a Raman-spectrum. Such a spectrum is shown in Fig. 4. The Stokes and anti-Stokes lines caused by scattering at GaAs-like TO-phonons are measured at the InAlGaAs/AlGaAs-waveguide of a high-power laser

array are indicated. First, the temperature dependence of the line position, see Fig. 5 (left) can serve for temperature determination. This shift is due to the change of the crystal lattice parameter with temperature. Second, one can take benefit of the fact that the energetic distribution of phonons follows Bose-Einstein statistics. Thus, independently from the line position, the parameter ‘temperature’ can be determined from the intensity ratio of Stokes- and anti-Stokes lines; see Fig. 5 (right). Thus both Figs. 5 can be seen as two independent calibration curves. Of course the saturation

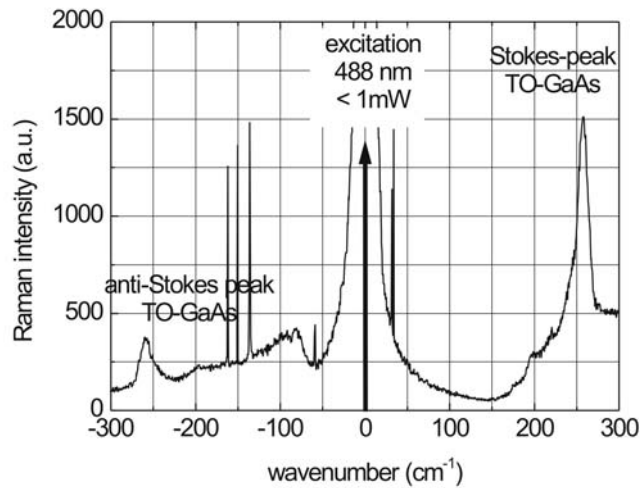


Fig. 4. Micro-Raman spectrum from the optical active region of an AlGaAs-based diode laser.

seen in Fig. 5 (right) is rather expected to converge towards 1. The deviation observed here is caused by the apparatus function, in particular by the notch filter used in this experiment.

In our following applications we determine the averaged bulk temperature within the laser cavity in the standard way from the spectral shift of the device emission wavelength. The emission wavelength of the device is simultaneously detected by the Raman setup from either the fundamental or second harmonic signal of the laser emission.

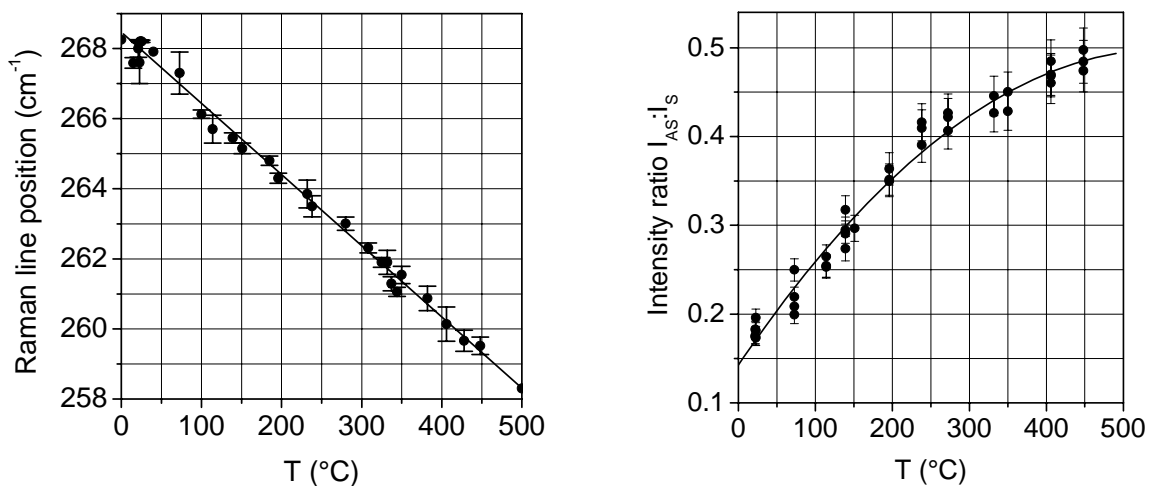


Fig. 5. Calibration curves for Raman facet temperature measurements. Spectral line position of the TO-GaAs-like mode (left) and anti-Stokes-Stokes line intensity ratio (right) versus temperature.

Now we come to an experiment carried out with large-optical-cavity step-index separate confinement heterostructure lasers grown by MBE. The 940 nm emitting devices are fabricated on the basis of an  $\text{In}_{0.12}\text{Ga}_{0.88}\text{As}/\text{Al}_{0.2}\text{Ga}_{0.8}\text{As}$  QW laser structure. Two kinds of laser diodes are made, first

standard lasers with a very short blocking layer (5  $\mu\text{m}$ ) on the front facet only and a second group of lasers where the blocking layer is reaching about 30  $\mu\text{m}$  into the laser. The blocking layers of the standard lasers are basically just for giving a cleaving mark, and not long enough to prevent current spreading from the contacted area to the facet. The epitaxial layers between the QW and the cap layers have a total thickness of about 2  $\mu\text{m}$ . Thus, the 30  $\mu\text{m}$  long blocking layers should effectively

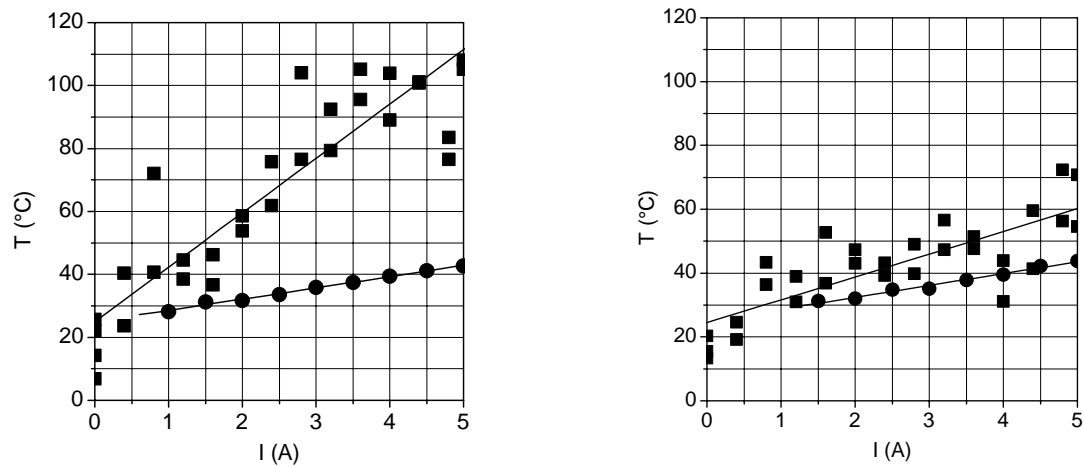


Fig. 6. Facet temperatures obtained by micro-Raman spectroscopy (squares) of two single QW InGaAs/-AlGaAs broad-area high-power laser-diodes. The circles mark averaged waveguide temperatures determined from the thermal emission wavelength shift (circles). The device, the data of which are presented on the right, has an additional 30  $\mu\text{m}$  wide current blocking layer at the front bottom contact.

prevent current spreading towards the facet. All devices are cleaved in a regular clean-room atmosphere. The high-reflectivity (R) facet is coated resulting in  $R=97\%$  whereas the emitting facet has  $R\sim 1\%$ . All lasers are 2 mm long, 200  $\mu\text{m}$  wide and mounted epi-side down on standard copper heat sinks (C-mounts). The facet treatment is the same for all lasers, and even the same wafer was used. The power-current-curves of both groups of lasers are identical. The slope, measured at 20  $^{\circ}\text{C}$  heatsink temperature in continuous wave mode, amounts around 1.06 W/A for all lasers, and the threshold current was around 0.71 A. If the heatsink temperature is increased to 50  $^{\circ}\text{C}$  the slope drops to 0.96 W/A and the threshold rises to 0.95 A. Figure 6 (left) displays facet and averaged waveguide temperature results for a standard device, whereas Fig. 6 (right) displays the result for a device with blocking layers. As expected from the similar standard laser parameters of devices from both groups, the averaged waveguide temperatures are almost similar as well. This is not surprising since a 30  $\mu\text{m}$  current blocking layer at a 2 mm long laser cavity (1.5 percent) should not affect its amplification properties too much. A striking difference, however, is seen for the facet temperatures where a reduction of the facet overheating by a factor of 4 is observed. Several reproducibility test with other pairs of lasers provide reductions by a factor between 3 and 4. Regardless of this impressive evidence of the success of a technological measure another very important conclusion may be drawn from this experiment. Since the optical load for the facets of both lasers is almost similar, it is clear that the facet heating is not caused by re-absorption of laser light. This important finding is in excellent agreement with former results obtained by other authors for QW lasers [16-18]. Surface currents are the most likely explanation [16-20].

The last experiment carried out with conventional high-power diode lasers involves the monitoring of facet temperatures within a long-term aging experiment. Fig. 7 (left) shows the evolution of the output power versus operation time for a 3 A operation current. The figure at the right presents facet temperatures versus operation current for three different operation times. Since the regular operation current for this type of devices is 2 A, this experiment is to be considered an accelerated aging test. Perhaps one is not too much surprised that when a slight drop of the emission power is visible after 4867 h of operation, one also observes an increased facet temperature; see full

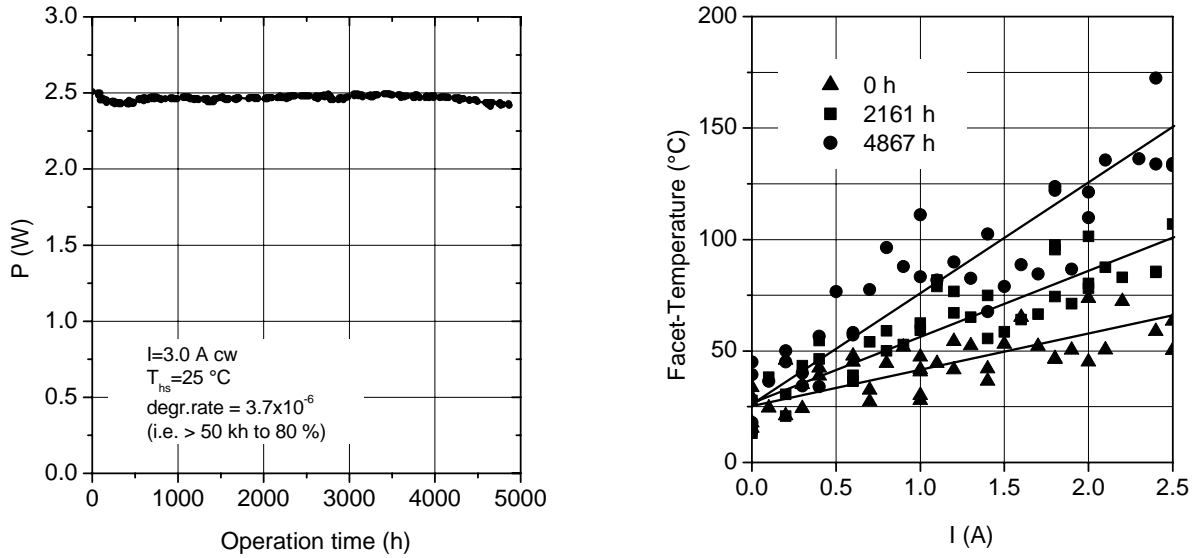


Fig. 7. The evolution of facet temperatures during device aging for an InAlGaAs double-QW high-power laser array. The figure at the left shows the output power versus operation time for 3 A operation current. The figure at the right presents facet temperatures versus operation current for three different aging times; compare with the left figure.

circles in Fig. 7 (right). On the other hand, it becomes also clear that even after only 2161 h of operation, when the output power shows still a perfect behavior, the facet temperature is already substantially increased; see full squares. Thus facet degradation appears as a gradual process, which starts a long time before any device parameter become indicative for degradation processes.

Diode lasers with a QD active layer offer a variety of advantages compared to conventional devices such as QW lasers [21]. Obviously, the reduced combined density of states reduces the lasing threshold. Another expected advantage is a lowered facet temperature due to a reduced number of non-equilibrium carrier pairs that might create heat by recombining non-radiatively at the facet. Among the mechanisms that potentially reduce the carrier population at the surface, there is the reduced in-plane diffusion coefficient within the QD-plane; see also the schematic diagram in Fig. 8 (left). The next experiment presented here is aimed to prove even this hypothesis. For this purpose we use two 1100 nm emitting QW- and QD-devices that are especially grown for this particular

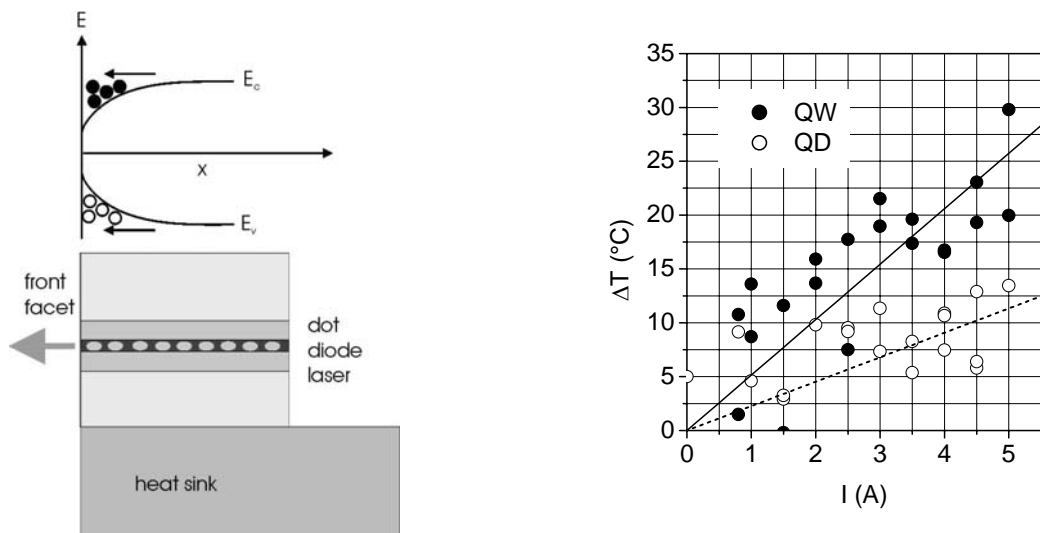


Fig. 8. Schematic diagram of a QD-laser (left bottom) and simplified band structure of the surface impacted by facet heating (left top). The right figure shows the facet overheating, i.e. facet temperature reduced by the averaged bulk temperature of a QW and a QD laser; see full and open circles, respectively.

experiment. The main idea underlying this experiment was to have two lasers, namely one QW- and one QD-device with absolutely the same design and properties except the active layer. Pre-characterization experiments have shown that the device vendor met this technological challenge [22]. In particular the light output characteristics are almost identical for both devices. For technological reasons, however, the devices were packaged p-side up. In order to protect the devices we decided to make the temperature measurement under pulsed excitation only. The data shown in Fig. 8 (right) represent the facet overheating, i.e. facet temperatures that are already reduced by the averaged waveguide temperatures. Thus we find for QW- and QD-lasers with an almost similar device design a reduction of the facet overheating by 40 to 60 percent for the QD devices. Since the surface treatments of both devices are similar we assign this finding to the ‘QD-effect’, most likely to the expected reduced in-plane diffusion in such structures.

## 6. CONCLUSIONS

We present a number of practical applications of Raman spectroscopy to device analysis. First we discuss effects of technological processes such as ion-implantation and rapid thermal annealing and their impact on Raman spectra. In the second part we address the use of micro  $\mu$ Raman spectroscopy for the analysis of strains along device structures. The third part is on the use of this technique as a unique ‘micro-thermometer’. After a methodological introduction into this kind of surface temperature measurement, a number of practical examples of  $\mu$ Raman investigations at facets of diode lasers are presented. We present the results of a Raman-spectroscopy based study of facet heating in different types of high-power diode lasers. Facet temperature data for cw and pulsed laser operation are presented. For conventional 940-nm emitting high-power broad area lasers we demonstrate the reduction of the facet overheating by the introduction of current blocking layers by a factor of 3-4. We demonstrate that facet heating is not caused by re-absorption of laser light. Surface currents are the most likely explanation for facet heating in these devices. For long-term aging experiments we show slightly increased facet temperatures in very early stages of the experiment, when all laser parameters are still undegraded. For another set of devices consisting of QW- and QD-lasers with an almost similar device design we find a reduction of the overheating by 40 to 60 percent for the QD devices. Thus we qualify two complementary promising technological approaches for increasing diode laser device reliability and demonstrate that  $\mu$ Raman spectroscopy is still a state-of-the-art tool for device analysis.

## References

1. H. YAMAZAKI AND K. WATANABE APPL. PHYS. LETT. 1994, **64**, 2540.
2. M. HOLZ, R. ZALLEN, ART E. GEISSBERGER, AND R. SADLER, J. APPL. PHYS. 1986, **59**, 1946.
3. J. WAGNER AND CH. HOFFMAN APPL. PHYS. LETT. 1987, **50**, 682.
4. M. HOLZ, R. ZALLEN, O. BRAFMAN, AND S. MATTESON PHYS REV. B 1988, **37**, 4609.
5. K. K. TIONG, P. M. AMIRTHARAJ, AND F. H. POLLAK, APPL. PHYS. LETT. 1984, **44**, 122.
6. P. VERMA, S. C. ABBI, AND K. P. JAIN, PHYS REV. B 1995, **51**, 16660.
7. E. ANASTASSAKIS AND J. TATARKIEWICZ, APPL. PHYS. LETT. 1987, **50**, 245.
8. G. LANDA, R. CARLES, C. FONTAINE, E. BEDEL, AND A. MUNOZ-YAGÜE J. APPL. PHYS. 1989, **66**, 196.
9. D. OLEGO, H. BAUMGART, AND G. K. CELLER, APPL. PHYS. LETT. 1988, **52**, 483.
10. P. S. PIZANI, A. MLAYAH, J. GROENEN, R. CARLES, AND A. CLAVERIE, APPL. PHYS. LETT. 1995, **66**, 1927.
11. M. BALKANSKI, R. F. WALLIS, AND E. HARO, PHYS REV. B 1983, **28**, 1928.
12. JENS W. TOMM, AXEL GERHARDT, ROLAND MÜLLER, MARK L. BIERMANN, JOSEPH P. HOLLAND, DIRK LORENZEN, AND EBERHARD KAULFERSCH, APPL. PHYS. LETT. 2003, **82**, 4193-4195.
13. J. W. TOMM, A. GERHARDT, R. MÜLLER, V. MALYARCHUK, Y. SAINTE-MARIE, P. GALTIER, J. NAGLE, AND J.-P. LANDESMAN, J. APPL. PHYS. **93**, 2003, 1354-1362.
14. G. LANDA, R. CARLES, C. FONTAINE, E. BEDEL, AND A. MUNOZ-YAGÜE, J. APPL. PHYS. 1989, **66**, 196.

15. J. W. TOMM, A. GERHARDT, T. ELSAESSER, D. LORENZEN, AND P. HENNIG, *APPL. PHYS. LETT.* 2002, **81** 3269-3271.
16. W. C. TANG, H. H. ROSEN, P. VETTINGER, AND D. J. WEBB, *APPL. PHYS. LETT.*, 1991, **59**, 1005-1007.
17. W. C. TANG, H. H. ROSEN, P. VETTINGER, AND D. J. WEBB, *APPL. PHYS. LETT.*, 1992, **60**, 1043-1045.
18. F. U. HERRMANN, S. BEECK, G. ABSTREITER, C. HANKE, C. HOYLER, AND L. KORTE, *APPL. PHYS. LETT.* 1991, **58**, 1007-1009.
19. G. BEISTER, J. MAEGE, D. GUTSCHE, G. ERBERT, J. SEBASTIAN, K. VOGEL, M. WEYERS, J. WÜRFL, AND O.P. DAGA, *APPL. PHYS. LETT.*, 1996, **68**, 2467-2468.
20. G. BEISTER, J. MAEGE, J. SEBASTIAN, G. ERBERT, L. WEIXELBAUM, M. WEYERS, J. WÜRFL, AND O.P. DAGA, *IEEE PHOT. TECH. LETT.* 1996, **8**, 1124-1126.
21. D. BIMBERG, M. GRUNDMANN, AND N. N. LEDENTSOV, *QUANTUM DOT HETEROSTRUCTURES*, JOHN WILEY & SONS, CHICHESTER, 1999.
22. J. W. TOMM, F. RINNER, E. THAMM, C. RIBBAT, R. SELLIN, AND D. BIMBERG, *SPIE PROC.* 2003, **4993**, 91-98.